

tions with TP antagonism, TP deletion also reduced the procedure-related increment in urinary Tx-M (Fig. 1D). To address the contribution of exaggerated Tx biosynthesis to the vascular proliferative response in IPKO mice, we studied coincidental deletion of the TP and the IP [TPIP double knockouts (DKOs)], which abolished the increased response to injury observed in the IPKOs (15) (Fig. 1, A, B, and D, and Web table 1). All three indices of proliferation were similar in TPIP DKOs and their WT littermates. Furthermore, the augmented, procedure-related increment in platelet activation, observed in IPKOs, was also abolished by concomitant TP and IP deletion (Fig. 1D).

Biosynthesis of PGI₂ is elevated along with TxA₂ in human syndromes of platelet activation (22, 23), and the formation and activity of the two prostaglandins may interact via several mechanisms. TP agonists evoke PGI₂ release from endothelial cells in vitro (24), and platelet-derived endoperoxide precursors of TxA₂ may also be utilized by endothelial COX to generate PGI₂ in vitro (25). Pharmacological inhibition of Tx synthase enhances redirection of endoperoxides to platelet inhibitory prostanoids, such as PGI₂, in vivo (26). Both the arachidonic acid in microparticles shed by activated platelets (27) and platelet-derived TxA₂ evoke COX-2-dependent PGI₂ formation by endothelial cells (28). Considerable evidence also exists for cross talk between IP- and TP-dependent signaling pathways. Thus, TP desensitization evokes sensitization to IP agonists (29), and IP activation evokes TP desensitization (30).

Our data establish that endogenous PGI₂ modulates the cardiovascular actions of TxA₂ in vivo. This interplay may be relevant to the cardiovascular effects of selective COX-2 inhibitors, which, unlike aspirin and NSAIDs, depress PGI₂ without coincidental inhibition of TxA₂ formed by COX-1 in platelets. Although our results suggest that the enhancement of the deleterious effects of TxA₂ is a plausible explanation for the cardiovascular outcome in the VIGOR trial, they do not exclude a contributory role for naproxen's cardioprotective effect. Indeed, both mechanisms may be important. If the estimate of the difference in incidence rates of myocardial infarction between the groups is accurate, it is roughly twice that expected if naproxen was affording cardioprotection via sustained inhibition of platelet COX-1 (31).

The response to carotid vascular injury was modified by both TP antagonism and TP deletion. Although our mouse models do not perfectly simulate percutaneous angioplasty on an atherosclerotic background in humans, it prompts reconsideration of the potential utility of TP antagonists in this setting. Two clinical trials have compared TP antagonists with aspirin for the prevention of restenosis after angioplasty (32, 33). TP antagonists, in contrast to aspirin, do not depress PGI₂ formation. Patients received periprocedural aspirin before randomization to

continuing aspirin or a TP antagonist for the following 6 months. However, the aspirin regimen used depresses the procedure-related increment in PGI₂ biosynthesis (16). Our results suggest that this may have conditioned the proliferative response to injury and may have undermined the comparison of the two treatments.

References and Notes

1. S. Moncada, R. Gryglewski, S. Bunting, J. R. Vane, *Nature* **263**, 663 (1976).
2. S. Bunting, R. Gryglewski, S. Moncada, J. R. Vane, *Prostaglandins* **12**, 897 (1976).
3. G. A. FitzGerald, B. Smith, A. K. Pedersen, A. R. Brash, *N. Engl. J. Med.* **310**, 1065 (1984).
4. G. A. FitzGerald, C. Patrono, *N. Engl. J. Med.* **345**, 433 (2001).
5. B. F. McAdam et al., *Proc. Natl. Acad. Sci. U.S.A.* **96**, 272 (1999).
6. F. Catella-Lawson et al., *J. Pharm. Exp. Ther.* **289**, 735 (1999).
7. J. N. Topper, J. Cai, D. Falb, M. A. Gimbrone Jr, *Proc. Natl. Acad. Sci. U.S.A.* **93**, 10417 (1996).
8. N. Ueno et al., *J. Biol. Chem.* **276**, 34918 (2001).
9. C. Bombardier et al., *N. Engl. J. Med.* **343**, 1520 (2000).
10. T. Namba et al., *J. Biol. Chem.* **269**, 9986 (1994).
11. M. Hirata et al., *Nature* **349**, 617 (1991).
12. T. Murata et al., *Nature* **388**, 678 (1997).
13. D. W. Thomas et al., *J. Clin. Invest.* **102**, 1994 (1998).
14. W. M. Cheung, M. R. D'Andrea, P. Andrade-Gordon, B. P. Damiano, *Arterioscler Thromb. Vasc. Biol.* **19**, 3014 (1999).
15. Supplementary material is available on Science Online at www.sciencemag.org/cgi/content/full/296/5567/539/DC1.

16. G. A. Braden, H. R. Knapp, G. A. FitzGerald, *Circulation* **84**, 679 (1991).
17. L. Schwartz et al., *N. Engl. J. Med.* **318**, 1714 (1988).
18. B. Cimetiere et al., *Bioorg. Med. Chem. Lett.* **8**, 1375 (1998).
19. B. Rocca et al., *Nature Med.* **6**, 219 (2000).
20. Y. Cheng, G. A. FitzGerald, unpublished observations.
21. M. L. Pedersen, M. Watson, G. A. FitzGerald, *Thromb. Res.* **35**, 99 (1983).
22. G. A. FitzGerald, *Am. J. Cardiol.* **68**, 11B (1991).
23. L. Roy, H. Knapp, R. M. Robertson, G. A. FitzGerald, *Circulation* **71**, 434 (1985).
24. N. S. Nicholson, S. L. Smith, G. C. Fuller, *Thromb. Res.* **35**, 183 (1984).
25. A. J. Marcus, B. B. Weksler, E. A. Jaffe, M. J. Broekman, *J. Clin. Invest.* **66**, 979 (1980).
26. J. Nowak, G. A. FitzGerald, *J. Clin. Invest.* **83**, 380 (1989).
27. O. P. Barry, D. Pratico, R. C. Savani, G. A. FitzGerald, *J. Clin. Invest.* **102**, 136 (1998).
28. G. E. Caughey, L. G. Cleland, J. R. Gamble, M. J. James, *J. Biol. Chem.* **276**, 37839 (2001).
29. R. Murray, L. Shipp, G. A. FitzGerald, *J. Biol. Chem.* **265**, 21670 (1990).
30. M. T. Walsh, J. F. Foley, B. T. Kinsella, *J. Biol. Chem.* **275**, 20412 (2000).
31. C. Patrono et al., *Chest* **119**, 395 (2001).
32. P. W. Serruys et al., *Circulation* **84**, 1568 (1991).
33. M. P. Savage et al., *Circulation* **92**, 3194 (1995).
34. We wish to thank P. McNamara and R. D. Rudic for advice and encouragement. We also thank S. Segel and H. Li for technical assistance. Supported in part by grants from Servier and the National Institutes of Health (HL 54500 and HL 62250). All procedures were considered and approved by Institutional Animal Care and Usage Committee of the University of Pennsylvania.

5 December 2001; accepted 28 February 2002

Optical Projection Tomography as a Tool for 3D Microscopy and Gene Expression Studies

James Sharpe,* Ulf Ahlgren, Paul Perry, Bill Hill, Allyson Ross, Jacob Hecksher-Sørensen, Richard Baldock, Duncan Davidson

Current techniques for three-dimensional (3D) optical microscopy (deconvolution, confocal microscopy, and optical coherence tomography) generate 3D data by "optically sectioning" the specimen. This places severe constraints on the maximum thickness of a specimen that can be imaged. We have developed a microscopy technique that uses optical projection tomography (OPT) to produce high-resolution 3D images of both fluorescent and nonfluorescent biological specimens with a thickness of up to 15 millimeters. OPT microscopy allows the rapid mapping of the tissue distribution of RNA and protein expression in intact embryos or organ systems and can therefore be instrumental in studies of developmental biology or gene function.

The ability to analyze the organization of biological tissue in three dimensions has proven to be invaluable in understanding embryo development, a complex process in which tissues undergo an intricate sequence of movements relative to each other. A relat-

ed goal is the mapping of gene expression patterns onto these 3D tissue descriptions (1). This information provides clues about the biological functions of genes and also indicates which genes may interact with each other. Gathering this data has become one of the clear challenges of the genomics era.

A number of techniques for obtaining 3D information about biological tissue have recently been developed or improved (2–7). Methods for the digital reconstruction of thin serial sections have become increasingly automated (2,

Medical Research Council, Human Genetics Unit, Western General Hospital, Crewe Road, Edinburgh EH4 2XU, UK.

*To whom correspondence should be addressed. E-mail: james.sharpe@hgu.mrc.ac.uk

REPORTS

Fig. 1. OPT microscopy. (A) A schematic of the OPT microscopy setup. The specimen is rotated within a cylinder of agarose while held in position for imaging by a microscope. Light transmitted from the specimen (blue lines) is focused by the lenses onto the camera-imaging chip (CIC). The apparatus is adjusted so that light emitted from a section that is perpendicular to the axis of rotation (red ellipse) is focused onto a single row of pixels on the CIC (red line). The section highlighted as a red ellipse in (A) is seen as a red circle in (B). The region of the specimen sampled by a single pixel of the CIC is shown as a double inverted cone shape (blue region). Points far from the focal plane will not appear sharply focused in the image (pale blue shading), while those closer to the plane will be more focused (darker blue shading). Although confocal microscopy attempts to minimize the noise from out-of-focus regions by illuminating only those points on the focal plane, in our experiments we made the sample cones as narrow as possible (17) so that the sampled region approximated a narrow cylinder through the specimen. Because the depth-of-focus was not always large enough to include the entire specimen, we adjusted the position of the axis of rotation so that only the front half of the specimen was in focus. This ensured that every part of the specimen was imaged in focus during a full 360 degree rotation (17). (C) The sampled regions from adjacent pixels were distributed across the section as an approximation of parallel line integrals.

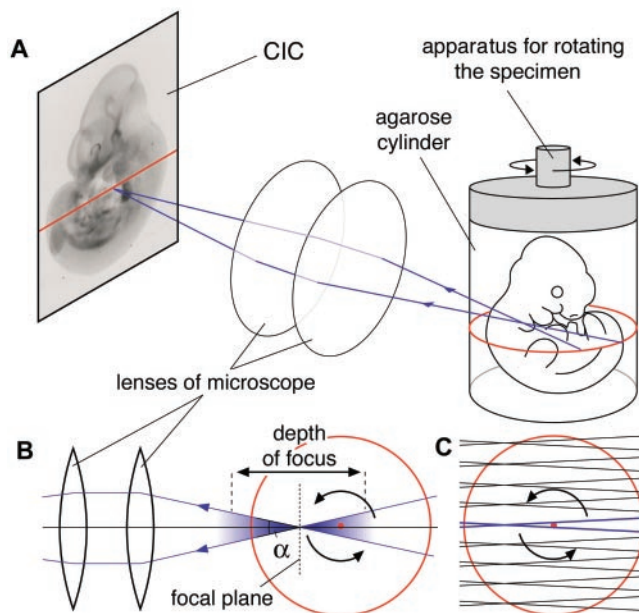
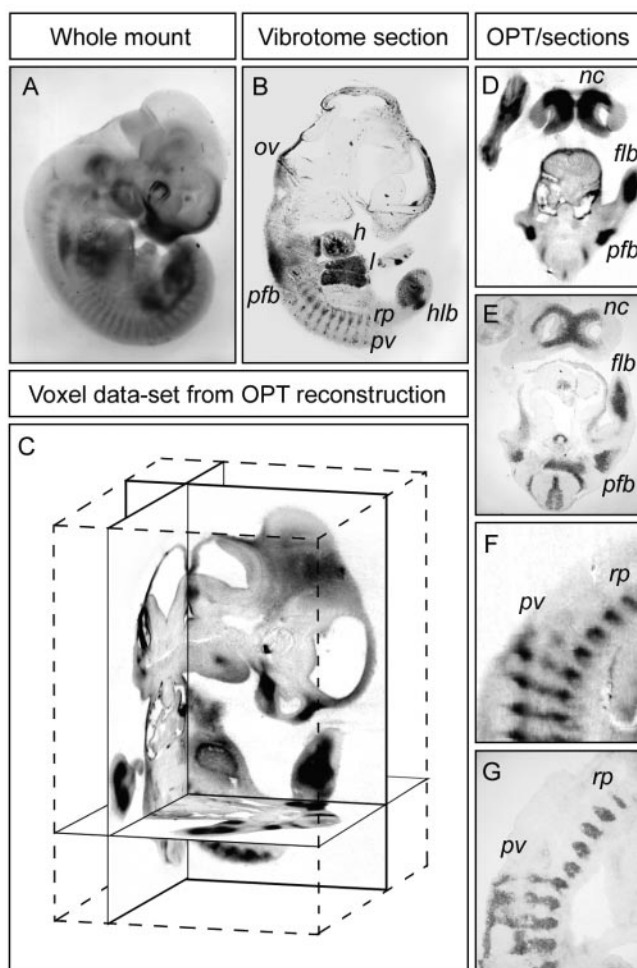


Fig. 2. 3D reconstruction of the Sox9 expression pattern. (A) An E11.5 mouse embryo whole-mount stained for expression of the Sox9 gene (in which the staining is clearly visible, but determining exactly which tissues are expressing is not possible). (B) A 50- μ m thick vibratome section cut through a similar whole-mount stained embryo, in which expression can be seen in the proximal forelimb bud (pfb), prevertebrae (pv), rib primordia (rp), hindlimb bud (hlb), and superficial region of the otic vesicle (ov). Dark blood can also be seen in the liver (l) and heart (h). (C) The 3D OPT reconstruction of the embryo shown in (A) [see (20)]. Virtual sections in three orthogonal planes are shown, within the context of the full 3D block of voxel data. The last column shows two comparisons between virtual OPT sections (D and F) and in situ hybridizations that were performed on cryostat sections (E and G). All the sites of expression shown in the OPT sections (around the nasal cavities, nc; the forelimb bud, flb; proximal limb bud, plb; prevertebrae, pv; rib primordia, rp; and around the heart) are shown in the corresponding cryostat sections. The cryostat staining shown just ventral to the neural tube is not shown in the OPT section, because that tissue was too deep for reagent penetration during the whole-mount staining procedure.



3), but reconstructing a specimen that is a few millimeters across still requires the cutting of hundreds of individual sections. Although confocal microscopy can image to a depth of approximately 1 mm, particularly in the case of the recently developed two-photon and multiphoton techniques (4), this is not sufficient to image many specimens intact. Additionally, confocal microscopy is limited to imaging only fluorescent signals, making it unsuitable for analysis of the colored dyes used in many biochemical assays [such as X-galactopyranoside (X-gal) detection of LacZ reporter gene activity, 5-bromo-4-chloro-3-indolyl phosphate/nitro blue tetrazolium (BCIP/NBT) detection of in situ hybridization, or placental alkaline phosphatase (PLAP) reporter gene activity]. Another 3D optical technique, optical coherence tomography (5), can image to greater depths than can confocal microscopy (up to 2 to 3 mm), but still cannot image complete mouse embryos. A nonoptical technique that shows great potential for developmental biology is microscopic magnetic resonance imaging (μ MRI) (6). High-contrast agents have recently been developed that allow the detection of LacZ reporter expression within living specimens (7). However, the complexity and expense of this technique, coupled with its inability to image commonly used assays, such as colored or fluorescent dyes, make it unsuitable for general application.

Tomographic reconstruction of an object is possible using information about sections of the object, projections of the object, or both. Current forms of 3D optical microscopy use the principle of section tomography; for instance, confocal microscopy generates "optical sections" through a specimen by focusing on a particular plane and minimizing noise coming from out-of-focus regions. This form of tomog-

REPORTS

raphy generates raw data that can be mapped directly into 3D space, because each discrete measurement relates to a volume element (called a voxel) in the final representation. By contrast, the raw data obtained in projection tomography must be mathematically transformed to recreate the original object (8). The most successful applications of projection tomography have been techniques like medical computerized tomography (CT) scans, in which the rays (x-rays in this case) are not significantly refracted or scattered when passing through biological tissue. The emerging field of diffuse optical tomography uses infrared wavelengths that can traverse as much as 10 cm of living biological tissue, but the resulting scattering of light means that only low-resolution reconstructions are possible (9).

High-resolution imaging using the principle of projection tomography requires that the raw data captured must approximate line integrals through the specimen. Although previous technologies (such as x-ray CT scanners) detect the unfocused shadow of the specimen, we wanted to explore whether an image-focusing optical system (such as a microscope) could be used to obtain suitable data, because this would allow standard fluorescent imaging to be performed in addition to brightfield imaging. An apparatus was constructed (10) that rotated a specimen through 360 degrees around a single axis while holding it in position for imaging (Fig. 1A). The specimens were supported in a transparent cylinder of agarose gel (1% low-melting-point) and rotated through angular steps of 0.9 degrees (11). A digital image of the static specimen was taken at each of the 400 rotated positions. To reduce scattering and refraction of light as it passed through the specimen, the rotating specimen was immersed in Murray's Clear during imaging (a 1:2 mixture of benzyl alcohol and benzyl benzoate). Figure 1 shows how the images taken approximated parallel projection data through the specimen. After the 400 images were taken, virtual sections were independently reconstructed using a back-projection algorithm (8), and high-resolution representations of sections through the specimen were produced.

The discovery that OPT microscopy could map the light-absorbing properties of tissue suggested that it might be possible to image the 3D distribution of gene expression patterns as revealed by in situ staining techniques. A standard protocol (10) was used to perform a whole-mount in situ hybridization on an E11.5 mouse embryo for mRNA expression of the *Sox9* gene (Fig. 2A) (12). The embryo was then prepared and scanned as for unstained specimens. Reconstruction of the embryo gave a detailed 3D description of the expression pattern (Fig. 2). The production of a 3D data set for the specimen meant that this single embryo could then be virtually sectioned in any orientation, allowing accurate determination of the sites of expression. The results were compared against those

from more traditional techniques (thick vibratome sectioning of whole-mount labeled embryos, and in situ hybridization performed on paraffin wax sections) (Fig. 2). All dark regions of the embryo were recorded in the OPT reconstruction (including the pigmented retina of the eye).

Fluorescence microscopy provides an ad-

vantage over normal light microscopy because one can use it to image multiple signals independently. We therefore tested whether the OPT approach could use fluorescent images as its raw data. We adapted fluorescence histochemistry protocols to allow the whole-mount staining of large specimens and imaged these with the OPT rotational stage, under a

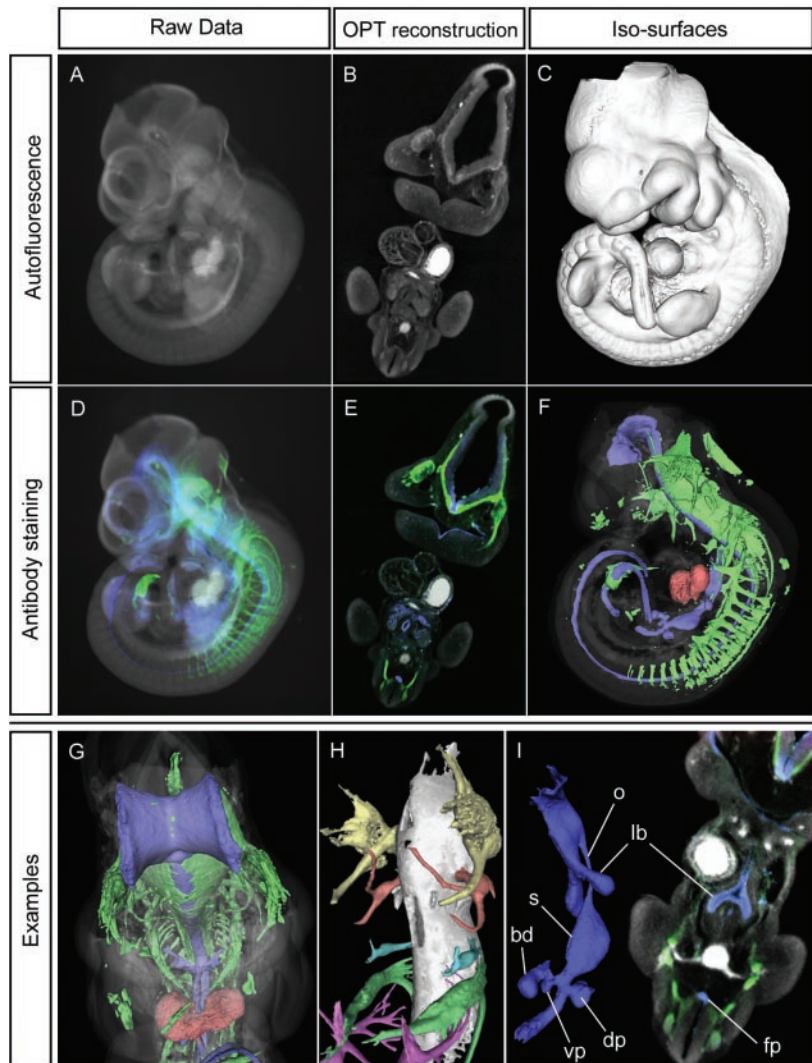


Fig. 3. Fluorescence OPT imaging of multiple signals within an E10.5 mouse embryo with HNF3 β antibodies labeling the floorplate of the neural tube and the endoderm and neurofilament antibodies labeling the developing nerve tracts [see (20)]. (A) One of the 400 images showing autofluorescence from the embryo. (B) A virtual section through the OPT-generated voxel data of the autofluorescent signal. (C) 3D rendering of an iso-surface generated from the voxel reconstruction of the autofluorescent signal. (D to F) The same three views as shown in (A) to (C), with the fluorescent data from the double-antibody staining included. Blue, HNF3 β ; green, neurofilament. In (F), the autofluorescent iso-surface has been rendered transparent so that the 3D shapes of the antibody staining patterns can be seen within the embryo, and the high autofluorescence of blood in the heart has been rendered in red. These 3D representations can be viewed from any angle, as seen in (G), which is a different view of the reconstruction shown in (F). (H) A close-up of the developing nerve tracts in the head of the embryo. The colors (which were manually "painted") of the ganglia are yellow, trigeminal (V); red, facial (VII); blue, glossopharyngeal (IX); green, vagus (X) and accessory (XI); and white, the ventral side of the neural tube [as seen in (F) and (H) as a green signal]. (I) Two representations of the same data. On the left is a 3D iso-surface representing the shape of the HNF3 β -expressing tissues (esophagus, o; lung buds, lb; stomach, s; dorsal and ventral pancreatic buds, dp and vp; and bile duct, bd). On the right, the same HNF3 β signal can be seen within the context of the whole embryo as a virtual section. HNF3 β expression can be seen in the lung buds (lb) and the floorplate (fp) (blue), and neurofilament expression can be seen in the nerve tracts (green).

REPORTS

dissecting microscope with fluorescent imaging capabilities. Figure 3 shows the images of an E10.5 embryo stained for HNF3 β and neuro-

filament proteins. Filter sets were chosen to selectively image the two fluorochromes used (Alexa 488 and Cy3), and a third set was used

to record the autofluorescence emitted by all the tissue. The images for each fluorescent channel were then used independently in three reconstruction calculations. Because the embryo was imaged in exactly the same position for each fluorescent channel, the three reconstructions could be mapped into the same 3D space.

Tissue-specific labeling by certain antibodies makes this process ideal for describing the 3D shape of developing embryonic organs. We used HNF3 β antibodies to label the developing endoderm and the floorplate of the spinal cord (13, 14), and we used neurofilament antibodies to label developing neurons. From the OPT reconstructions, we could view the signals as virtual sections (Fig. 3, B and E), which could be cut through the data in any orientation. Alternatively, 3D iso-surfaces (contours that connect all regions above a certain threshold intensity) could be generated to illustrate the shapes of the signal, and therefore the shapes of the tissues in which they were expressed (Fig. 3, F to I). Using suitable software, these surfaces could be rotated and examined from any angle, rendered in different colors or varying degrees of transparency, and combined to illustrate their spatial relationships to each other (Fig. 3 F and G).

We explored whether OPT microscopy could reveal aspects of mutant morphology that would be hard to detect by other means. The asplenic phenotype of *Bapx1(Nkx3.2)* null mice has been described previously (15–17); however, on closer examination, we observed a slightly abnormal overall shape of the developing stomach, which has not been previously reported. We performed whole-mount immunohistochemistry on the isolated foregut region from E13.5 embryos, using antibodies against the E-cadherin protein, which is expressed in the endodermal component of the developing esophagus, stomach, pancreas, and duodenum (as well as other structures) (Fig. 4, A to D). Figure 4, E to H, illustrates how the results from OPT microscopy allow a simple, direct comparison of morphology between wild-type and mutant specimens. This analysis highlights the fact that the posterior walls of the mutant stomachs are lined with grooves and ridges, a feature not previously reported (18). If physical sections alone had been used for this analysis, the undulations in the ventral side of the stomach might have been considered to be an artifact caused by mounting the sections onto glass slides (a process that invariably introduces some distortion of the tissue).

Although good anatomical and morphological descriptions of embryo development form one of the foundations for developmental biology, our knowledge is far from complete. The speed and convenience of OPT microscopy raises the possibility of a new phase of 3D descriptive embryology. 3D reconstructions of shapes such as the developing nervous system (Fig. 3) would be difficult, if not impossible, using any published techniques. Confocal microscopy cannot image through a whole em-

Fig. 4. The use of OPT microscopy in reassessing wild-type and mutant morphology. Fluorescent immunohistochemistry of E-cadherin expression on dissected gastrointestinal tracts from E13.5 embryos. (A) Photograph showing one image of the 400 angles taken of a control specimen. The bright signal corresponds to specific staining of the endoderm, whereas the weaker signal is nonspecific fluorescence from the surrounding mesenchyme (dorsal pancreas, dp; spleen, spl; duodenum, d; ventral pancreas, vp; pyloric sphincter, ps; stomach, s; esophagus, o). (B) OPT reconstruction of the dorsal pancreas showing the convoluted shapes of the developing lobules. (C) The surface reconstruction of the whole dissected tissue [colored regions correspond to close-ups in panels (B) and (D)]. The apparent hole in the side of the stomach illustrates the effect of different threshold values for the iso-surface. It occurs because that region of endoderm expresses E-cadherin at a lower level than is expressed in the rest of the stomach. If a lower threshold value is chosen for the iso-surface, then no hole is seen (E). (D) Close-up of the dual pancreatic ducts connected to both the duodenum below and the fused pancreatic tissue above. (E) View of a wild-type stomach wall and a corresponding section (F) [represented by the green section plane in (E)]. (G) Close-up of the same region [panel (E)] of a *Bapx1* mutant stomach showing significant ridges and grooves. The virtual section shown in (H) [green plane in (G)] shows two ridges (white arrowheads) that are prominent in the 3D surface rendering (black arrowheads).

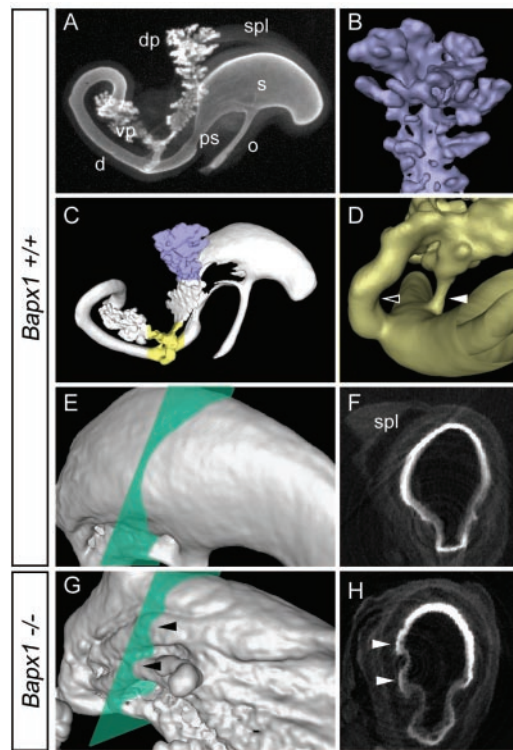
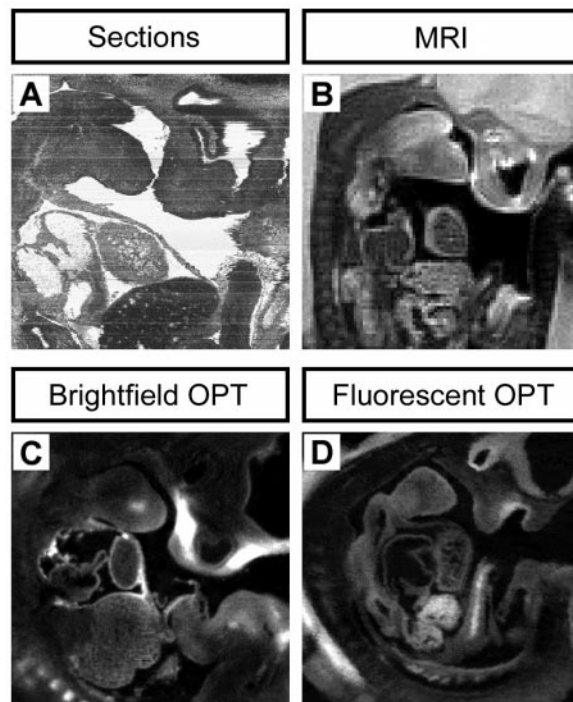


Fig. 5. Comparison of OPT microscopy with other 3D reconstruction techniques. (A) 3D reconstruction of an E12.5 mouse embryo generated from paraffin wax sections. (B) A similar sagittal section through a voxel data set of an E11.5 mouse embryo, generated by μ MRI [courtesy of R. Jabobs (21)]. Although the contrast between adjacent structures is high, the resolution is not sufficient to clearly identify all the internal organs. (C) A virtual sagittal section through an E11.5 mouse embryo generated by OPT microscopy using brightfield images. (D) A similar section through an E10.5 mouse embryo generated by fluorescent OPT microscopy. In both fluorescent and brightfield OPT imaging, the resolution is higher than that from μ MRI, although the alignment of the data is better than the alignment produced by serial sections (because it is a nondestructive imaging technique). The effective resolution of OPT is 5 to 10 μ m, which is indicated by the fact that single-cell membranes (which are about 10- μ m thick) can clearly be seen. Fluorescent OPT generally produces sharper images than does brightfield OPT [as seen in the comparison between internal organs in (D) versus (C)].



bryo, magnetic resonance imaging does not capture data at high enough resolution (Fig. 5), and serial sections cannot be aligned well enough to recreate structures as fine as nerve fibers (19). Any colored stain can be imaged in the same way as the in situ analysis shown in Fig. 2, allowing for the 3D visualization of results from many other types of experiments (for example, tissue-specific activity of enhancers and promoters in LacZ reporter constructs, cell lineage studies, and gene-trap experiments). The main disadvantage of OPT microscopy, as compared to μ MRI, is that high-resolution reconstructions depend on the specimen being transparent and its tissues possessing a homogenous refractive index.

The increasing demand for comprehensive gene expression data has led to the creation of large-scale bioinformatics databases, some of which aim to store data on the 3D expression patterns of thousands of genes (1). We believe OPT microscopy will dramatically increase the rate at which such data is gathered as well as facilitate the detailed examination of mutant phenotypes from large-scale mutagenesis screens.

In addition to its use in developmental biology, OPT microscopy has the potential for use in medical applications for which knowledge of the 3D structure of a specimen may be useful, but not readily accessible from histopathological sections.

References and Notes

1. D. Davidson, R. Baldock, *Nature Rev. Genet.* **2**, 409 (2001).
2. W. J. Weninger, T. Mohun, *Nature Genet.* **30**, 59 (2001).
3. J. Streicher *et al.*, *Nature Genet.* **25**, 147 (2000).
4. S. M. Potter, S. E. Fraser, J. Pine, *Scanning* **18**, 147 (1996).
5. S. A. Boppart, M. E. Brezinski, B. E. Bouma, G. J. Tearney, J. G. Fujimoto, *Dev. Biol.* **177**, 54 (1996).
6. R. E. Jacobs, S. E. Fraser, *Science* **263**, 681 (1994).
7. A. Y. Louie *et al.*, *Nature Biotechnol.* **18**, 321 (2000).
8. A. C. Kak, M. Slaney, *Principles of Computerized Tomographic Imaging* (IEEE Press, 1988).
9. K. Chen, L. T. Perelman, Q. Zhang, R. R. Dasari, M. S. Feld, *J. Biomed. Opt.* **5**, 144 (2000).
10. International patents pending.
11. Detailed materials, methods, and a further characterization of the system are described on Science Online at www.sciencemag.org/cgi/content/full/296/5567/541/DC1.
12. E. Wright, *Nature Genet.* **9**, 15 (1995).
13. A. Ruiz i Altaba, V. R. Prezioso, J. E. Darnell, T. M. Jessell, *Mech. Dev.* **44**, 91 (1993).
14. U. Ahlgren, J. Jonsson, H. Edlund, *Development* **122**, 1409 (1996).
15. L. Lettice *et al.*, *Proc. Natl. Acad. Sci. U.S.A.* **96**, 9695 (1999).
16. M. Tribioli, T. Lufkin, *Development* **126**, 5699 (1999).
17. Akazawa *et al.*, *Genes Cells* **5**, 499 (2000).
18. U. Ahlgren, J. Sharpe, J. Hecksher-Sorensen, N. Hastie, R. Hill, unpublished data.
19. The method described in (2) aligns sections well enough, but as yet cannot image specific fluorescent signals such as those from antibody staining.
20. Movies showing these 3D results and more information about the technique can be found online at http://genex.hgu.mrc.ac.uk/OPT_Microscopy.
21. M. Dhenain, S. Ruffins, R. E. Jacobs, *Dev. Biol.* **232**, 458 (2001).
22. We thank C. Sy and L. Hay for help in developing the

device; R. Bryson-Richardson, M. Stark, A. Ijpenberg, D. Fitzpatrick, and R. Hill for useful discussions on the technique; and N. D. Hastie for strong support of the project. HNF3 β antibodies were a gift from T. E. Jessell. Funded by a Medical Research Council Training Fellow-

ship (J.S.), the Swedish Foundation for International Cooperation in Higher Research and Education (U.A.), and the Danish Research Academy (J.H.S.).

19 November 2001; accepted 5 March 2002

Divergent Regulation of Dihydrofolate Reductase Between Malaria Parasite and Human Host

Kai Zhang and Pradipsinh K. Rathod*

For half a century, successful antifolate therapy against *Plasmodium falciparum* malaria has been attributed to host-parasite differences in drug binding to dihydrofolate reductase–thymidylate synthase (DHFR-TS). Selectivity may also arise through previously unappreciated differences in regulation of this drug target. The DHFR-TS of *Plasmodium* binds its cognate messenger RNA (mRNA) and inhibits its own translation. However, unlike translational regulation of DHFR or TS in humans, DHFR-TS mRNA binding is not coupled to enzyme active sites. Thus, antifolate treatment does not relieve translational inhibition and parasites cannot replenish dead enzyme.

Malaria caused by various species of protozoan parasites, *Plasmodium*, results in about 900 million acute cases and 2.7 million deaths every year (1). With the emergence of drug resistance, there is a continual need for new antimalarial agents that are potent and selective. Development of new drugs will be greatly facilitated by a complete understanding of the molecular mechanisms underlying previously successful antimalarials. Antifolates, including pyrimethamine, have been used in the treatment of malaria for about 50 years (2). These drugs target DHFR-TS, a specific bifunctional protein in the parasite (3). DHFR and TS are expressed as separate proteins in mammalian cells, but the functional importance, if any, of the difference seen in the protein configuration has remained elusive.

The selective activity of pyrimethamine has traditionally been attributed to higher affinity of the drug for *Plasmodium* DHFR-TS than for human DHFR (2, 4–6). However, other DHFR-TS inhibitors, which lack parasite-specific affinity, also show selective toxicity for malaria (7–9). WR99210 is a potent inhibitor of *P. falciparum* proliferation in culture (median inhibitory concentration $IC_{50} = 0.1$ nM; Fig. 1A) (9, 10). In contrast, human fibroblast HT1080 cells tolerate this compound ($IC_{50} = 6300$ nM; Fig. 1A) (10). The large difference in sensitivity to WR99210 is not due to differential affinity for DHFR: Enzyme kinetic assays

revealed a mere 10-fold difference in binding of WR99210 between *Plasmodium* DHFR-TS (inhibition constant $K_i = 1.1$ nM) and human DHFR ($K_i = 12$ nM) (10). Integration of one human DHFR coding sequence in *P. falciparum* is sufficient to shift the IC_{50} of WR99210 from 0.1 nM to 860 nM, as previously reported (11, 12). This degree of resistance is similar to that of human cells (Fig. 1A). Thus, WR99210 selectivity does not arise from host-parasite differences in drug uptake, metabolism, or export.

Host-parasite differences in the regulation and expression of DHFR and TS may play a role in drug selectivity. Mammalian DHFR and TS levels increase with specific drug treatment (13–15): Methotrexate causes accumulation of DHFR protein (13), and 5-fluorouracil and D1694 increase TS levels (15, 16). Translational control determines such drug-induced target overproduction in mammalian cells. In the absence of substrates or drugs, mammalian DHFR and TS bind their cognate mRNA within the coding region and block translation (16–18). In the presence of substrates [dihydrofolate (DHF) and the reduced form of nicotinamide adenine dinucleotide phosphate (NADPH) for DHFR; deoxyuridine monophosphate (dUMP) and 5,10-methylenetetrahydrofolate (mTHF) for TS] or inhibitors [methotrexate for DHFR; 5-fluoro-dUMP (FdUMP) for TS], the host enzymes disassociate from their cognate mRNA, relieving translational arrest (16–18). Thus, drug treatment reverses natural, autologous, translational inhibition and causes overproduction of the target protein. Such innate cellular buffering ensures that mammalian cells are resistant to inhibitors of DHFR and TS. The absence of such cellular buffering may ac-

Department of Chemistry, University of Washington, Seattle, WA 98195, USA, and Seattle Biomedical Research Institute, Seattle, WA 98109, USA.

*To whom correspondence should be addressed. E-mail: rathod@chem.washington.edu